

# Unsteady Heat and Fluid Flow through a Curved Channel with Rectangular Cross-section for Several Cases of Aspect Ratio

Samir Chandra Ray<sup>a\*</sup>, Rabindra Nath Mondal<sup>b</sup>

<sup>a</sup>*Department of Mathematics, Bangabandhu Sheikh Mujibur Rahman Science and Technology University,  
Gopalganj-8100, Bangladesh*

<sup>b</sup>*Department of Mathematics, Jagannath University, Dhaka-1100, Bangladesh  
Email: Samir.math@bsmrstu.edu.bd*

## Abstract

In this paper, a comprehensive numerical study is presented for the fully developed two-dimensional flow of viscous incompressible fluid through a curved rectangular duct with different aspect ratios 2 and 3 for a constant curvature  $\delta = 0.1$ . Unsteady solutions are obtained by using a spectral method and covering a wide range of Dean number  $100 \leq Dn \leq 1000$  and the Grashof number  $1000 \leq Gr \leq 2000$ . The outer wall of the duct is heated while the inner wall is cooled. The main concern of this study is to find out the unsteady flow behavior *i.e* whether the unsteady flow is steady-state, periodic, multi-periodic or chaotic, if the Dean number or the Grashof number is changed. For the aspect ratio 2, it is found that the unsteady flow is a steady-state solution for  $Dn = 100$  and  $Gr = 100, 500, 1500, 2000$  but periodic at  $Dn = 100$  and  $Gr = 1000$ . If the Dean number is increased *i.e.* at  $Dn = 500$ , it is found the unsteady flow is periodic at  $Gr = 1000, 1500$  but chaotic at  $Gr = 100, 500, 2000$ . If the Dean number is increased further *i.e.* at  $Dn = 1000$ , the unsteady flow becomes chaotic for any value of  $Gr$  in the range. For the aspect ratio 3, however, it is found that the unsteady flow is a steady-state solution for  $Dn = 100$  at  $Gr = 100$  and  $Gr = 2000$  but periodic at  $Dn = 100$  and  $Gr = 500, 1000, 1500$ . If the Dean number is increased *i.e.* at  $Dn = 500$  and  $1000$ , the unsteady flow becomes chaotic for any value of  $Gr$  in the range. Contours of secondary flow patterns and temperature profiles are also obtained, and it is found that the unsteady flow consists of a single-, two-, three-, four-, five-, six-, seven- and eight-vortex solutions. It is also found that the chaotic flow enhances heat transfer more significantly than the steady-state or periodic solutions as the Dean number are increased.

**Keywords:** Curved rectangular duct; secondary flow; unsteady solutions; Dean number; Taylor number; Grashof number; time evolution.

---

\* Corresponding author.

## 1. Introduction

Fluid flow through curved ducts and channels has been extensively studied over a wide range of applications because of their enormous applications in fluids engineering. Such motivation has provided a fairly comprehensive knowledge of physics and numerical modeling addressing intrinsic vortex-structure promoting mixing and momentum transfer. Now a days, flows in curved ducts channels are extensively used in many engineering applications, such as in turbo-machinery, refrigeration, air conditioning systems, heat exchangers, rocket engine, internal combustion engines and blade-to-blade passages in modern gas turbines. Dean [1] was the first who formulated the problem in mathematical terms under the fully developed flow conditions and showed the existence of a pair of counter rotating vortices in a curved pipe. The readers are referred to [2–5] for some outstanding reviews on curved duct flows.

The fluid flow in a rotating curved duct generates centrifugal and Coriolis force. Such rotating passages are used in many engineering applications e.g. in cooling system for conductors of electrical generators. For isothermal flows of a constant property fluid, the Coriolis force tends to generate vortices while centrifugal force is purely hydrostatic by (Zhang and his colleagues [6]). An early complete bifurcation study of two-dimensional (2-D) flow through a curved duct of square cross section was conducted by Winters [7]. He determined that the isolated symmetric 4-cell sub-branch is unstable while the isolated 2-cell sub branch is stable. The location of limit point and bifurcation points does not change much for curvature ratios less than 0.02, but at higher curvature ratios, they move to large  $Dn$  numbers. Mondal and his colleagues [8] performed comprehensive numerical study on fully developed bifurcation structure and stability of two-dimensional (2D) flow through a curved duct with square cross section and found a close relationship between the unsteady solutions and the bifurcation diagram of steady solutions. When a temperature induced variation of fluid density occurs for non-isothermal flows, centrifugal type buoyancy forces can contribute to the generation of vorticity [9]. These effects counteract each other in a non-linear manner depending on the direction of wall, resistance coefficients and the flow domain. Therefore, the effect of counteract of the system is more subtle and complicated and yields new; richer features of flow and heat transfer in general, bifurcation and stability in particular, for non-isothermal flows.

Time dependent analysis of fully developed curved duct flows was initiated by Yanase and Nishiyama [10] for a rectangular cross section. In that study, they investigated unsteady solutions for the case where dual solutions exist. The time-dependent behavior of the flow in a curved rectangular duct of large aspect ratio was investigated, in detail, by Yanase and his colleagues [5] numerically. They performed time-evolution calculations of the unsteady solutions with and without symmetry condition and showed that periodic oscillations appear with symmetry condition while aperiodic time variation without symmetry condition. Wang and Liu [11] performed numerical as well as experimental investigations of periodic oscillations for the fully developed flow in a curved square duct. Flow visualization in the range of Dean numbers from 50 to 500 was conducted in their experiment. They showed, both experimentally and numerically, that a temporal oscillation takes place between symmetric/asymmetric 2-cell and 4-cell flows when there are no stable steady solutions. Recently, Mondal and his colleagues [12] applied spectral method to study non-isothermal flow through a

curved rectangular duct of aspect ratios 1 to 3 and showed that the steady-state flow turns into chaotic flow through various flow instabilities if the aspect ratio is increased. They also showed that the chaotic solution becomes weak for small  $Dn$ 's, while strong for large  $Dn$ 's. However, solution structure as well as transient behavior of the unsteady solution is not yet resolved for the flow through a curved rectangular duct with bottom wall heating and cooling from the ceiling, which motivated the present study to fill up this gap.

One of the most important applications of curved duct flow is to enhance the thermal exchange between two sidewalls, because it is possible that the secondary flow may convey heat and then increases heat flux between two sidewalls. Chandratilleke and Nursubyakto [13] presented numerical calculations to describe the secondary flow characteristics in the flow through curved rectangular ducts that were heated on the outer wall, where they studied for small Dean numbers and compared the numerical results with their experimental data. Norouzi and his colleagues [14] investigated inertial and creeping flow of a second-order fluid with convective heat transfer in a curved square duct by using finite difference method. Chandratilleke and his colleagues [15] presented a numerical investigation to examine the secondary vortex motion and heat transfer process in fluid flow through curved rectangular ducts of aspect ratios 1 to 6. The study formulated an improved simulation model based on 3-dimensional vortex structures for describing secondary flow and its thermal characteristics. Zhang and his colleagues [16] adopted finite volume method and SIMPLE algorithm to perform laminar and turbulent flow through a curved square duct at low Reynolds number. There was a good agreement between their numerical result and the experimental data.

**Recently**, Mondal and his colleagues [17] investigated combined effects of centrifugal and Coriolis instability of the isothermal/non-isothermal flows through a rotating curved rectangular duct numerically. The secondary flow characteristics in a curved square duct were investigated experimentally by using visualization method by Yamamoto and his colleagues [18]. Three-dimensional incompressible viscous flow and heat transfer in a rotating U-shaped square duct were studied numerically by Nobari and his colleagues [19]. However, Unsteady Heat and Fluid Flow through a Curved Channel with Rectangular Cross-section for Various Aspect Ratios is not yet resolved. **Very recently**, Li and his colleagues [20] conducted a combined experimental and numerical study on 3D flow development in a curved rectangular duct with varying curvature. The flow fields were measured using Particle Image Velocimetry (PIV) and the numerical simulations were performed by solving the Reynolds Averaged Navier–Stokes (RANS) equations. Effects of curvature, Reynolds number and aspect ratio on Dean instability were discussed in that paper to accurately determine the core of secondary base vortices. To the best of the authors' knowledge, however, there has not yet been done any substantial work studying the solution structure as well as effects of unsteady solutions for the non-isothermal flow through a curved rectangular duct whose bottom wall is heated and cooling from the ceiling. But from the scientific as well as engineering point of view it is quite interesting because this type of flow is often encountered in engineering applications such as in gas turbines, metallic industry etc.

Examining the unique features of secondary flow and heat transfer, the main objective of the present study is to investigate time-dependent behavior of the unsteady solutions through a curved rectangular duct where outer wall of the duct is heated while the inner wall is cooled.

## 2. Flow Model and Mathematical Formulations

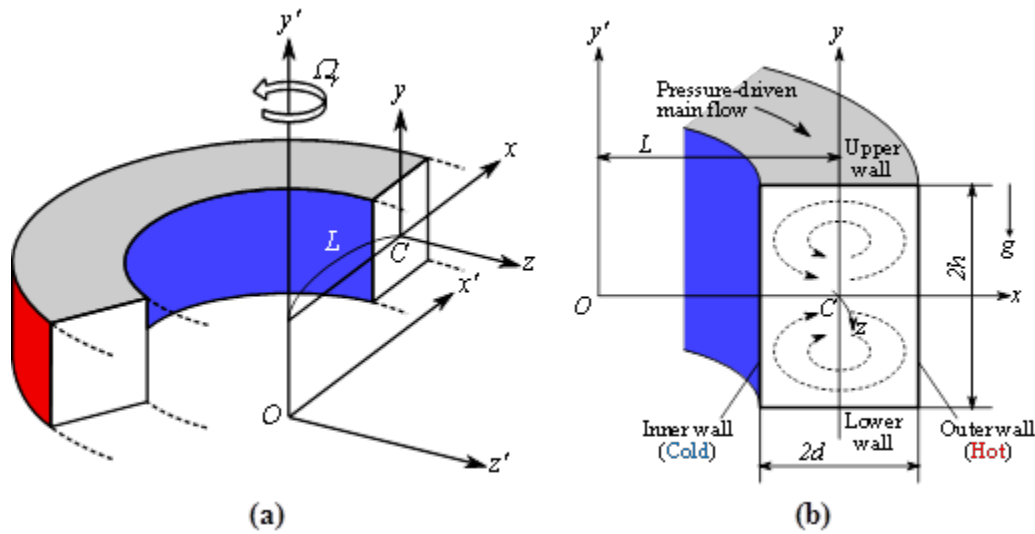


Figure 1: Coordinate system of the curved rectangular duct

Consider a hydro-dynamically and thermally fully developed two-dimensional (2D) flow of viscous incompressible fluid through a curved square duct, whose height or width are  $2d$ . The coordinate system with the relevant notation is shown in Figure 1, where  $x'$  and  $y'$  axes are taken to be in the horizontal and vertical directions respectively, and  $z'$  is the axial direction. It is assumed that the lower (bottom) wall of the duct is heated while the upper (top) wall is cooled. The temperature of the lower wall is  $T_0 + \Delta T$  and that of the upper wall is  $T_0 - \Delta T$ , where  $\Delta T > 0$ . It is also assumed that the flow is uniform in the axial direction, and that it is driven by a constant pressure gradient along the center-line of the duct. The dimensional variables are made non-dimensional by using the representative length  $d$ , the representative velocity  $U_0 = \frac{\nu}{d}$ , where  $\nu$  is the kinematic viscosity of the fluid. We introduce the non-dimensional variables defined as

$$u = \frac{u'}{U_0}, \quad v = \frac{v'}{U_0}, \quad w = \frac{\sqrt{2\delta}}{U_0} w', \quad x = \frac{x'}{d}, \quad y = \frac{y'}{d}, \quad z = \frac{z'}{d}$$

$$T = \frac{T'}{\Delta T}, \quad t = \frac{U_0}{d} t', \quad \delta = \frac{d}{L}, \quad P = \frac{P'}{\rho U_0^2}, \quad G = -\frac{\partial P'}{\partial z'} \frac{d}{\rho U_0^2}$$

where  $u, v$  and  $w$  are the non-dimensional velocity components in the  $x, y$  and  $z$  directions, respectively;  $t$  is the non-dimensional time,  $P$  is the non-dimensional pressure,  $\delta$  is the non-dimensional curvature defined as  $\delta = \frac{d}{L}$ , and temperature is non-dimensionalized by  $\Delta T$ . Henceforth, all the variables are non-dimensionalized if not specified.

Since the flow field is uniform in the  $z$  direction, the sectional stream function  $\psi$  is introduced as

$$u = \frac{1}{1 + \delta x} \frac{\partial \psi}{\partial y} \quad \text{and} \quad v = -\frac{1}{1 + \delta x} \frac{\partial \psi}{\partial x} \tag{1}$$

Then, the basic equations for  $w$ ,  $\psi$  and  $T$  are expressed in terms of non-dimensional variables as

$$(1 + \delta x) \frac{\partial w}{\partial t} + \frac{\partial(w, \psi)}{\partial(x, y)} - Dn + \frac{\delta^2 w}{1 + \delta x} = (1 + \delta x) \Delta_2 w - \frac{\delta}{1 + \delta x} \frac{\partial \psi}{\partial y} w + \delta \frac{\partial w}{\partial x} \tag{2}$$

$$\left( \Delta_2 - \frac{\delta}{1 + \delta x} \frac{\partial}{\partial x} \right) \frac{\partial \psi}{\partial t} = -\frac{1}{(1 + \delta x)} \frac{\partial(\Delta_2 \psi, \psi)}{\partial(x, y)} + \frac{\delta}{(1 + \delta x)^2} \left[ \frac{\partial \psi}{\partial y} \left( 2\Delta_2 \psi - \frac{3\delta}{1 + \delta x} \frac{\partial \psi}{\partial x} + \frac{\partial^2 \psi}{\partial x^2} \right) - \frac{\partial \psi}{\partial x} \frac{\partial^2 \psi}{\partial x \partial y} \right] \\ + \frac{\delta}{(1 + \delta x)^2} \times \left[ 3\delta \frac{\partial^2 \psi}{\partial x^2} - \frac{3\delta^2}{1 + \delta x} \frac{\partial \psi}{\partial x} \right] - \frac{2\delta}{1 + \delta x} \frac{\partial}{\partial x} \Delta_2 \psi + w \frac{\partial w}{\partial y} + \Delta_2^2 \psi - Gr(1 + \delta x) \frac{\partial T}{\partial x} \tag{3}$$

$$\frac{\partial T}{\partial t} + \frac{1}{(1 + \delta x)} \frac{\partial(T, \psi)}{\partial(x, y)} = \frac{1}{Pr} \left( \Delta_2 T + \frac{\delta}{1 + \delta x} \frac{\partial T}{\partial x} \right) \tag{4}$$

where,

$$\Delta_2 \equiv \frac{\partial^2}{\partial x^2} + \frac{\partial^2}{\partial y^2}, \quad \frac{\partial(T, \psi)}{\partial(x, y)} \equiv \frac{\partial f}{\partial x} \frac{\partial g}{\partial y} - \frac{\partial f}{\partial y} \frac{\partial g}{\partial x} \tag{5}$$

The equations for  $w, \psi$  and  $T$  are actually benefited for numerical computation. The non-dimensional parameters  $Dn$ , the Dean number;  $Gr$ , the Grashof number; and  $Pr$ , the Prandtl number, which appear in equation (2) to (4) are defined as:

$$Dn = \frac{Gd^3}{\mu\nu} \sqrt{\frac{2d}{L}}, \quad Gr = \frac{\beta g \Delta T d^3}{\nu^2}, \quad Pr = \frac{\nu}{\kappa} \tag{6}$$

where  $\mu, \beta, \kappa$  and  $g$  are the viscosity, the coefficient of thermal expansion, the co-efficient of thermal diffusivity and the gravitational acceleration respectively is the viscosity of the fluid. In the present study, only  $Dn$  and  $\delta$  are varied while  $Gr$  and  $Pr$  are fixed as,  $Gr = 100$  and  $Pr = 7.0$  (water).

The rigid boundary conditions for  $w$  and  $\psi$  are

$$w(\pm 1, y) = w(x, \pm 1) = \psi(\pm 1, y) = \psi(x, \pm 1) = \frac{\partial \psi}{\partial x}(\pm 1, y) = \frac{\partial \psi}{\partial y}(x, \pm 1) = 0 \tag{7}$$

and the temperature  $T$  is assumed to be constant on the walls as

$$T(x,1) = 1, \quad T(x,-1) = -1, T(\pm 1, y) = y \tag{8}$$

There is a class of solutions which satisfy the following symmetry condition with respect to the horizontal plane  $y = 0$ .

$$\left. \begin{aligned} w(x, y, t) &\Rightarrow w(x, -y, t), \\ \psi(x, y, t) &\Rightarrow -\psi(x, -y, t), \\ T(x, y, t) &= -T(x, -y, t) \end{aligned} \right\} \tag{9}$$

The solution which satisfies the condition (9) is called a *symmetric solution*, and that which does not an *asymmetric solution*. Note that, Equations (2) to (4) are invariant under the transformation of the variables

$$\left. \begin{aligned} y &\Rightarrow -y \\ w(x, y, t) &\Rightarrow w(x, -y, t), \\ \psi(x, y, t) &\Rightarrow \psi(x, -y, t), \\ T(x, y, t) &\Rightarrow -T(x, -y, t) \end{aligned} \right\} \tag{10}$$

Therefore, the case of heating the upper wall and cooling from the bottom can be deduced directly from the results obtained in this study.

### 3. Numerical Calculations

#### 3.1. Method of numerical calculation

In order to solve the Equations (2) to (4) numerically, the spectral method is used. This is the method which is thought to be the best numerical method for solving the Navier-Stokes as well as energy equations [21]. By this method the variables are expanded in a series of functions consisting of the Chebyshev polynomials. That is, the expansion functions  $\phi_n(x)$  and  $\psi_n(x)$  are expressed as

$$\left. \begin{aligned} \phi_n(x) &= (1-x^2) C_n(x), \\ \psi_n(x) &= (1-x^2)^2 C_n(x) \end{aligned} \right\} \tag{11}$$

where,  $C_n(x) = \cos(n \cos^{-1}(x))$  is the  $n^{th}$  order Chebyshev polynomial.  $w(x, y, t)$ ,  $\psi(x, y, t)$  and  $T(x, y, t)$  are expanded in terms of the expansion functions  $\phi_n(x)$  and  $\psi_n(x)$  as:

$$w(x, y, t) = \sum_{m=0}^M \sum_{n=0}^N w_{mn}(t) \phi_m(x) \phi_n(y) \tag{12}$$

$$\psi(x, y, t) = \sum_{m=0}^M \sum_{n=0}^N \psi_{mn}(t) \psi_m(x) \psi_n(y) \tag{13}$$

$$T(x, y, t) = \sum_{m=0}^M \sum_{n=0}^N T_{mn}(t) \varphi_m(x) \varphi_n(y) - y \tag{14}$$

where  $M$  and  $N$  are the truncation numbers in the  $x$  and  $y$  directions respectively, and  $w_{mn}, \psi_{mn}$  and  $T_{mn}$  are the coefficients of expansion. To obtain the steady solution, the time derivative terms  $\frac{\partial w}{\partial t}, \frac{\partial \psi}{\partial t}$ , and  $\frac{\partial T}{\partial t}$  are taken to be zero and the expansion series (12) - (14) with coefficients  $w_{mn}, \psi_{mn}$  and  $T_{mn}$ , being time independent, are substituted into the basic Eqs. (2), (3) and (4), and the collocation method (Gottlieb and Orszag, 1977) is applied. As a result, a set of nonlinear algebraic equations for  $w_{mn}, \psi_{mn}$  and  $T_{mn}$  are obtained. The collocation points  $(x_i, y_j)$  are taken to be

$$\left. \begin{aligned} x_i &= \cos \left[ \pi \left( 1 - \frac{i}{M+2} \right) \right], & i &= 1, K, M+1 \\ y_j &= \cos \left[ \pi \left( 1 - \frac{j}{N+2} \right) \right], & j &= 1, K, N+1 \end{aligned} \right\} \tag{15}$$

where  $i = 1, K, M+1$  and  $j = 1, K, N+1$ . Steady solutions are obtained by the Newton-Raphson iteration method assuming that all the coefficients to be time independent. To avoid difficulty near the point of inflection for the steady solutions, we use the arc-length method [22]. In the arc-length method, the arc-lengths play a central role in the formulation. The arc-length equation is

$$\sum_{m=0}^M \sum_{n=0}^N \left\{ \left( \frac{dw_{mn}}{ds} \right)^2 + \left( \frac{d\psi_{mn}}{ds} \right)^2 + \left( \frac{dT_{mn}}{ds} \right)^2 \right\} = 1 \tag{17}$$

The convergence is assured by taking sufficiently small  $\epsilon_p$  ( $\epsilon_p < 10^{-10}$ ) defined as

$$\epsilon_p = \sum_{m=0}^M \sum_{n=0}^N \left[ (w_{mn}^{(p+1)} - w_{mn}^p)^2 + (\psi_{mn}^{(p+1)} - \psi_{mn}^p)^2 + (T_{mn}^{(p+1)} - T_{mn}^p)^2 \right]. \tag{18}$$

Finally, in order to calculate the unsteady solutions, the Crank-Nicolson and Adams-Bashforth methods together with the function expansion (12) to (14) and the collocation methods are applied to equations (2) to (4).

### 3.2. Resistance coefficient

The resistant coefficient  $\lambda$  is used as the representative quantity of the flow state. It is also called the *hydraulic resistance coefficient*, and is generally used in fluids engineering, defined as

$$\frac{P_1^* - P_2^*}{\Delta_{z^*}} = \frac{\lambda}{d_h^*} \frac{1}{2} \rho \langle \omega^* \rangle^2 \quad (19)$$

where quantities with an  $P_1^*$  be asterisk denote dimensional ones,  $\langle \rangle$  stands for the mean over the cross section of the duct and  $d_h^*$  is the hydraulic diameter. The main axial velocity  $\langle \omega^* \rangle$  is calculated by

$$\langle \omega^* \rangle = \frac{v}{4\sqrt{2\delta}l} \int_{-1}^1 dx \int_{-1}^1 \omega(x, y, t) dy \quad (20)$$

Since  $(P_1^* - P_2^*)/\Delta_{z^*} = G$ ,  $\lambda$  is related to the mean non-dimensional axial velocity  $\langle \omega \rangle$  as

$$\lambda = \frac{4\sqrt{2\delta}Dn}{\langle \omega \rangle^2}, \quad (21)$$

where  $\langle \omega \rangle = \sqrt{2\delta}l \langle \omega^* \rangle / v$ . Equation (21) will be used to find the resistance coefficient of the flow evolution by numerical calculations.

## 4. Results and Discussion

In this study, we have investigated time evolution of the resistance coefficient  $\lambda$  for the fluid flows through a curved channel with rectangular cross-section for the curvature  $\delta = 0.1$ . We have studied the unsteady solutions of the flows at various Dean Numbers ( $Dn$ ) for two cases of the aspect ratios; **Case I:** aspect ratio  $l = 2$ , **Case II:** aspect ratio  $l = 3$ . In addition to the time evolution of  $\lambda$ , the secondary flow patterns and temperature profiles at various Dean numbers are also discussed in detail.

### 4.1. Case I: Aspect Ratio $l = 2$

#### 4.1.1. Time evolution of the unsteady solution

We investigate time evolution of  $\lambda$  for  $Dn = 100, 500$  and  $1000$  over a wide range of the Grashof number  $Gr$ ,  $100 \leq Gr \leq 2000$  for aspect ratio  $l = 2$ . In this section, we present the unsteady solutions for  $Dn = 100$  at  $Gr = 100, 500, 1500, 2000$ , and we find that the unsteady flow is periodic for  $Dn = 100, Gr = 1000$  and  $Dn = 500, Gr = 1000$ . We found that the unsteady flow is multi-periodic for  $Dn = 500$  at  $Gr = 1500$ . We obtained the chaotic solution for  $Dn = 500$  at  $Gr = 100, 500, 2000$ . We also obtained the chaotic solution for

$Dn = 1000$  and Gr number varies from  $100 \leq Gr \leq 2000$ .

Time evolution of the resistance coefficient  $\lambda$  at time  $20 \leq t \leq 30$  for  $Dn = 100$  and  $Gr = 100, 500, 1500, 2000$  for  $l = 2$  are shown in Fig 3(a), 4(a), 6(a), 7(a) respectively. It is found that the flow is steady-state for these cases. Secondary flow patterns and temperature profiles are shown in Fig 3(b), 4(b), 6(b), 7(b) for  $Dn = 100$  and  $Gr = 100, 500, 1500, 2000$  respectively. Here it is seen that the solution oscillates between symmetric one and two vortex solutions. To draw the contours of  $\psi$  and  $T$  for the aspect ratio  $l = 2$ , we use the increments  $\Delta\psi = 0.7$  and  $\Delta T = 0.2$ , respectively. The same increments of  $\psi$  and  $T$  are used for all the figures in this study for  $l = 2$ , unless specified. The right-hand side of each duct box of  $\psi$  and  $T$  is in the outside direction of the duct curvature. In the figures of the secondary flows, solid lines ( $\psi \geq 0$ ) show that the secondary flow is in the counter clockwise direction while the dotted lines ( $\psi < 0$ ) in the clockwise direction. Similarly, in the figures of the temperature field, solid lines are those for  $T \geq 0$  and dotted ones for  $T < 0$ . We investigate time evolution of the resistance coefficient  $\lambda$  at time  $20 \leq t \leq 40$  for  $Dn = 100$  and  $Gr = 1000$  as shown in Fig 5(a). We find that the flow is periodic for this case. From the contours of secondary flow and temperature profiles we observe that the unsteady flow is two-vortex solution, which is shown in Fig 5(b). In order to see the periodic oscillation more clearly, the phase space of the time evolution of  $\lambda$  is shown in Fig 5(c).

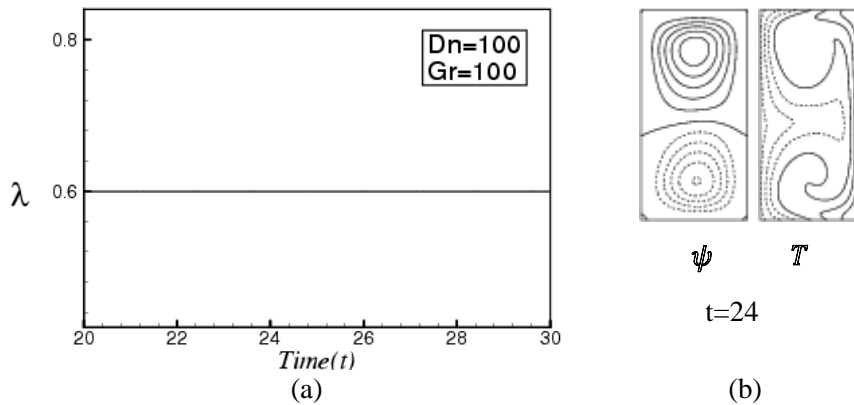


**Figure 2:** (a) Time evolution of  $\lambda$  at time  $20 \leq t \leq 30$ , (b) Secondary flow patterns (left) and Temperature profiles (right) for  $Dn = 100$  and  $Gr = 100, l = 2$  at time  $t = 24$

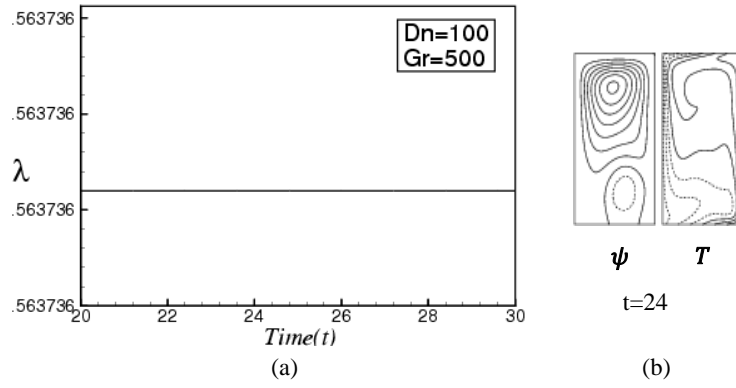


**Figure 3:** (a) Time evolution of  $\lambda$  at time  $20 \leq t \leq 30$ , (b) Secondary flow patterns (left) and Temperature profiles (right) for  $Dn = 500$  and  $Gr = 100, l = 2$  at time  $t = 24$

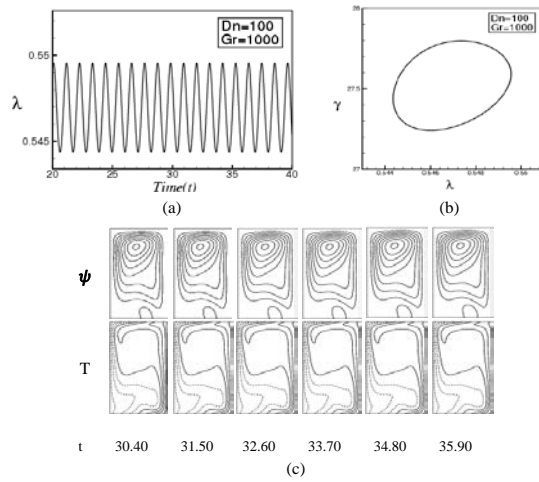


**Figure 4:** (a) Time evolution of  $\lambda$  at time  $20 \leq t \leq 40$ , (b) Phase space for  $Dn = 100$  and  $Gr = 1000, l = 2$ , (c) Secondary flow patterns (top) and Temperature profiles (bottom) for one period of oscillation for same  $Dn, Gr$  and  $l$  at time  $30.40 \leq t \leq 35.90$ .

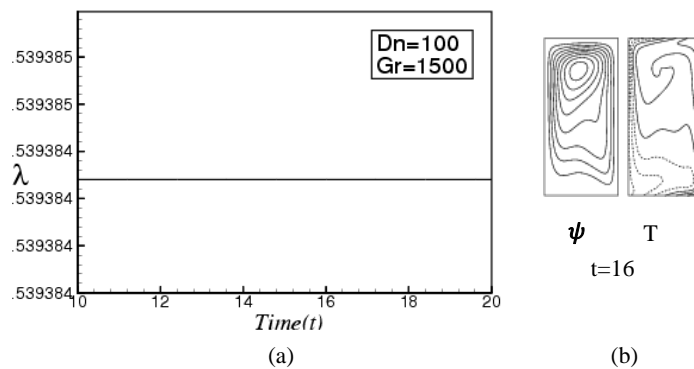


**Figure 5:** (a) Time evolution of  $\lambda$  at time  $10 \leq t \leq 20$ , (b) Secondary flow patterns (left) and Temperature profiles (right) for  $Dn = 100$  and  $Gr = 1500, l = 2$  at time  $t = 16$

profiles (right) for  $Dn = 100$  and  $Gr = 1500, l = 2$  at time  $t = 16$

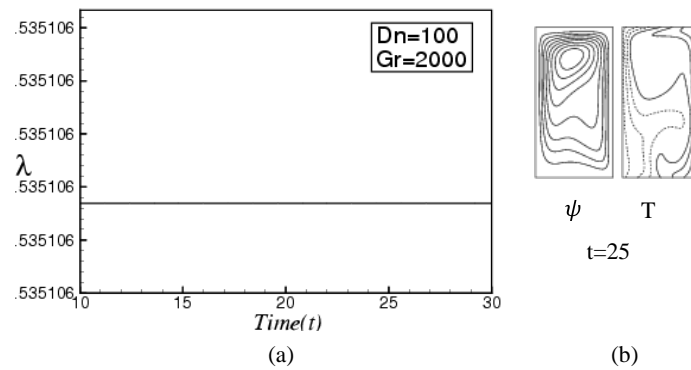


**Figure 6:** (a) Time evolution of  $\lambda$  at time  $10 \leq t \leq 30$ , (b) Secondary flow patterns (left) and Temperature profiles (right) for  $Dn = 100$  and  $Gr = 2000, l = 2$  at time  $t = 25$

Time evolutions of  $\lambda$  for  $Dn = 500, Gr = 100$  and  $Dn = 500, Gr = 500$  are shown in Fig 8(a), 9(a) respectively. It is found the solution is chaotic for both the cases. Secondary flow patterns and temperature profiles are shown in Fig 8(b) and 9(b) respectively. As seen in Figs. 8(b) and 9(b), the unsteady flow is symmetric two-, three- and four-vortex solutions. In order to see the chaotic behavior more clearly, the phase space of the time evolution of  $\lambda$  is also obtained as shown in Figs. 8(c) and 9(c) respectively. It is found that the unsteady solution of the flow is periodic for  $Dn = 500$  and  $Gr = 1000$  at time  $20 \leq t \leq 26$  as shown in Fig 10(a). Secondary flow patterns and temperature profiles are shown in Fig 10(b). We observe that asymmetric three-vortex solution is available. In order to see the periodic behavior more clearly, the phase space of the time evolution of  $\lambda$  is shown in Fig. 10(c). It is also found that the unsteady solution of the flow is multi-periodic for  $Dn = 500$  and  $Gr = 1500$  at time  $27 \leq t \leq 29$  as shown in Fig. 11(a). Secondary flow patterns and temperature profiles are shown in Fig. 11(b). We observe asymmetric two vortex solutions for this case. In order to see the periodic behavior more clearly, the phase space of the time evolution of  $\lambda$  is obtained as shown in Fig. 11(c). Time evolution of the resistance coefficient  $\lambda$  at time  $2 \leq t \leq 10$  for  $Dn = 500$  and  $Gr = 2000$  is shown in Fig. 12(a). We found that the flow is chaotic for  $Dn = 500$  and  $Gr = 2000$  at  $l = 2$ . Secondary flow patterns and temperature profiles are shown in Fig. 12(b). Here we found that there occur symmetric two- and three-vortex solutions. In order to see the chaotic behavior in more clearly, the phase space of the time evolution of  $\lambda$  is also shown in Fig. 12(c).

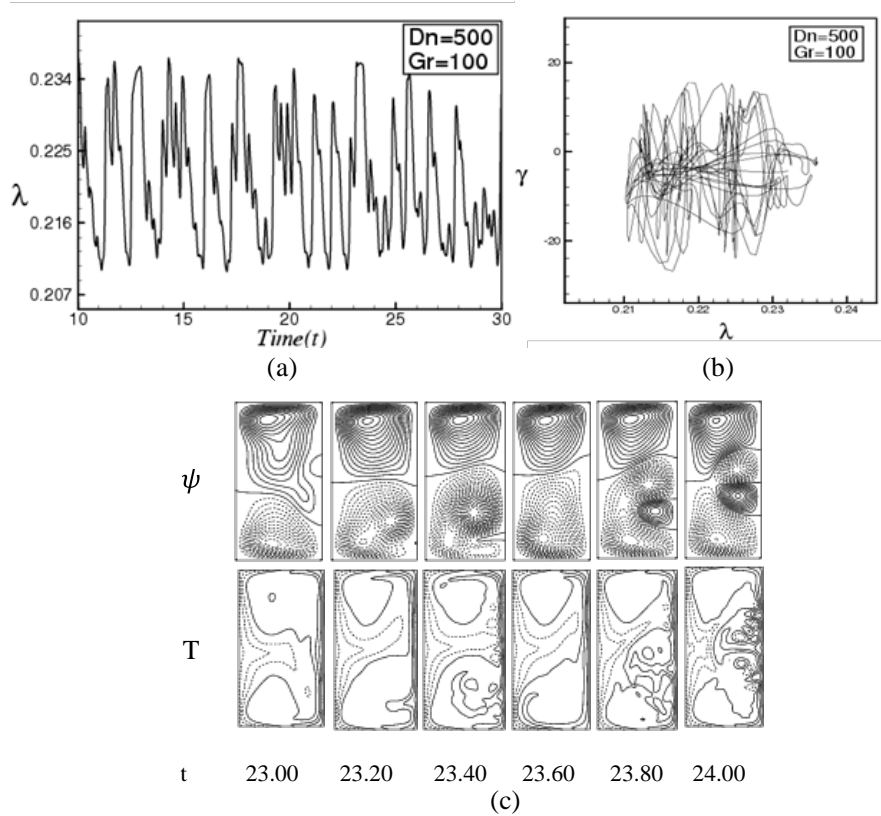


**Figure 7:** (a) Time evolution of  $\lambda$  at time  $10 \leq t \leq 30$ , (b) Phase space for  $Dn = 500$  and  $Gr = 100, l = 2$ , (c) Secondary flow patterns (top) and Temperature profiles (bottom) for one period of oscillation for same  $Dn, Gr$  and  $l$  at time  $23.00 \leq t \leq 24.00$ .

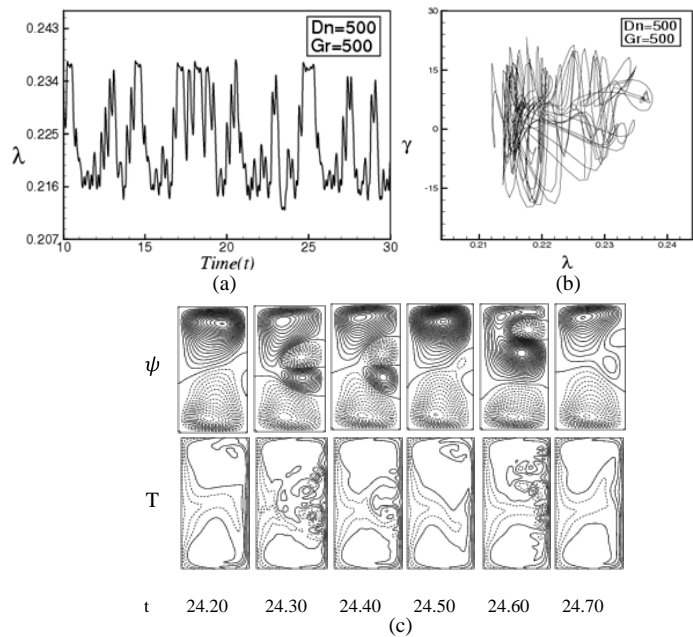


**Figure 8:** (a) Time evolution of  $\lambda$  at time  $10 \leq t \leq 30$ , (b) Phase space for  $Dn = 500$  and  $Gr = 500, l = 2$ ,

(c) Secondary flow patterns (top) and Temperature profiles (bottom) for one period of oscillation for same  $Dn, Gr$  and  $l$  at time  $24.20 \leq t \leq 24.70$ .

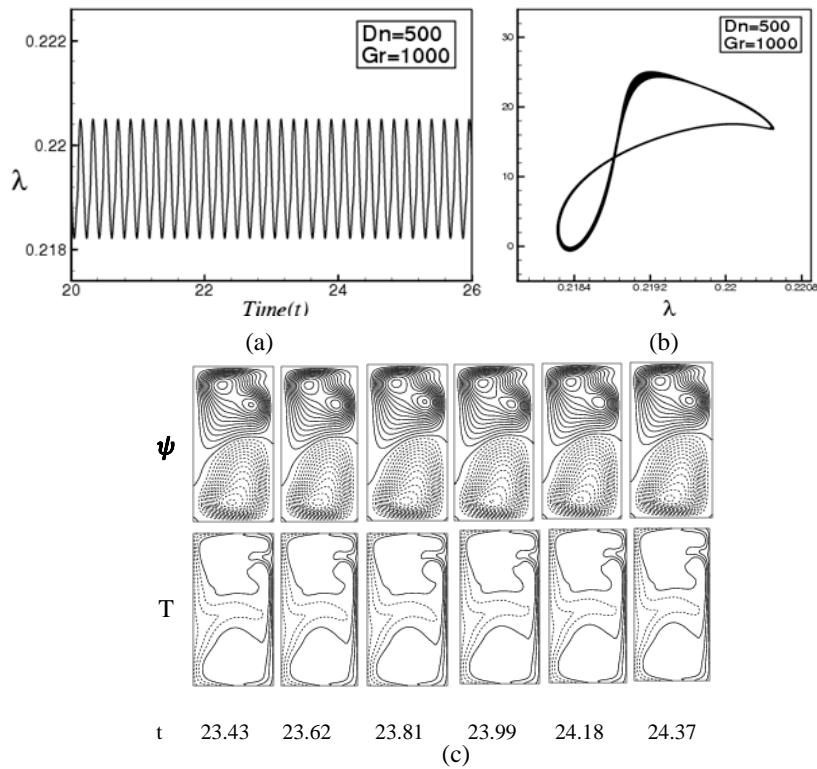


**Figure 9:** (a) Time evolution of  $\lambda$  at time  $10 \leq t \leq 30$ , (b) Phase space for  $Dn = 500$  and  $Gr = 1000, l = 2$ , (c) Secondary flow patterns (top) and Temperature profiles (bottom) for one period of oscillation for same  $Dn, Gr$  and  $l$  at time  $23.43 \leq t \leq 24.37$ .

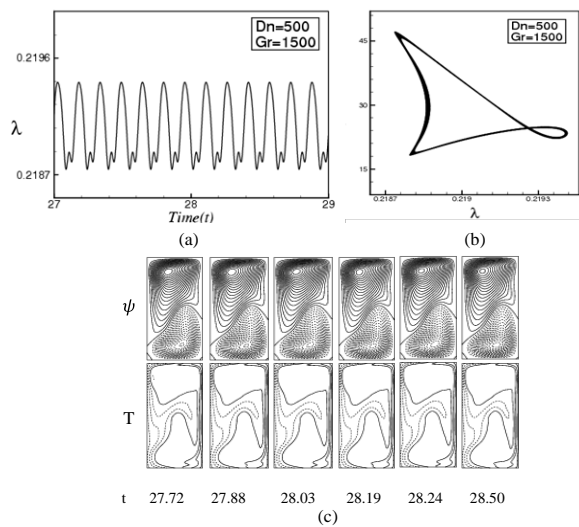


**Figure 10:** (a) Time evolution of  $\lambda$  at time  $27 \leq t \leq 29$ , (b) Phase space for  $Dn = 500$  and  $Gr = 1500, l = 2$ , (c) Secondary flow patterns (top) and Temperature profiles (bottom) for one period of oscillation for

same  $Dn, Gr$  and  $l$  at time  $27.72 \leq t \leq 28.50$ .

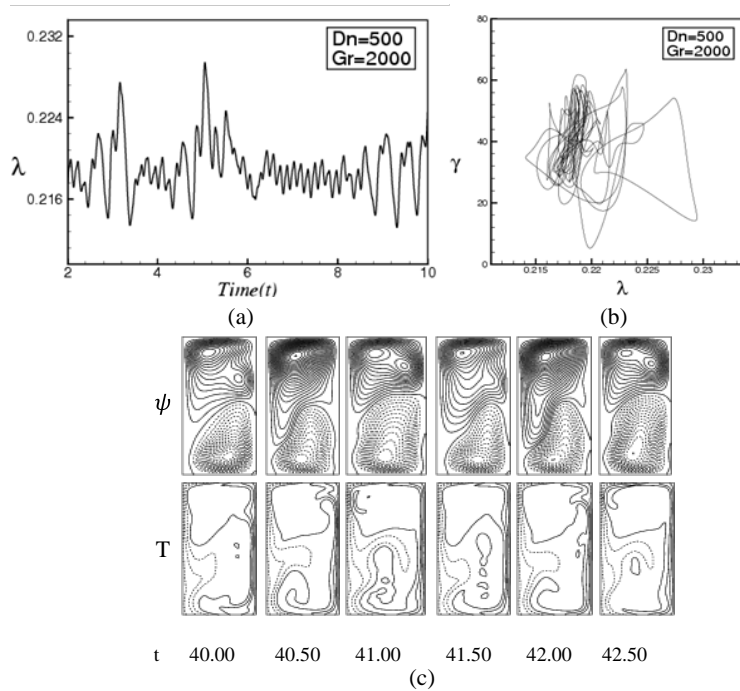


**Figure 11:** (a) Time evolution of  $\lambda$  at time  $2 \leq t \leq 10$ , (b) Phase space for  $Dn = 500$  and  $Gr = 2000, l = 2$ , (c) Secondary flow patterns (top) and Temperature profiles (bottom) for one period of oscillation for same  $Dn, Gr$  and  $l$  at time  $40.00 \leq t \leq 42.50$ .

Time evolution of the resistance coefficient  $\lambda$  at time  $20 \leq t \leq 30$  for  $Dn = 1000$  and  $Gr = 100$  is shown in Fig. 13(a). We found that the solution is chaotic. Secondary flow patterns and temperature profiles are shown in Fig. 13(b). As seen in Fig. 13(b), the unsteady flow is symmetric five- and six-vortex solutions. In order to see the chaotic behavior more clearly, the phase space of the time evolution of  $\lambda$  is shown in Fig. 13(c). Unsteady solution of the flow is chaotic for  $Dn = 1000$  and  $Gr = 500$  at time  $15 \leq t \leq 25$  is shown in Fig 14(a). Secondary flow patterns and temperature profile is shown in Fig 14(b), where we observe that the flow is asymmetric four-, five- and six-vortex solution. In order to see the chaotic behavior more clearly, the phase space of the time evolution of  $\lambda$  is also drawn as shown in Fig. 14(c). Time evolution of  $\lambda$  at time  $10 \leq t \leq 20$  for  $Dn = 1000$  and  $Gr = 1000, 1500$  is shown in Fig 15(a), 16(a) respectively for the aspect ratio 2 and we find that the unsteady solutions are chaotic. Secondary flow patterns and temperature profiles are shown in Figs. 15(b) and 16(b) respectively. Here we found symmetric four-, five- and six-vortex solutions. We also drew the phase spaces of the time evolution of  $\lambda$  as shown in Figs. 15(c) and 16(c) respectively. It is found that the unsteady solution of the flow is chaotic for  $Dn = 1000$  and  $Gr = 2000, l = 2$  is shown in Fig. 17(a). Secondary flow patterns and temperature profiles are shown in Fig. 17(b), where we observe that the flow is an asymmetric four- and five- vortex solution. In order to see the chaotic behavior more clearly, the phase space of the time evolution of  $\lambda$  is obtained as shown in Fig. 17(c) for for  $Dn = 1000$  and  $Gr = 2000, l = 2$ .

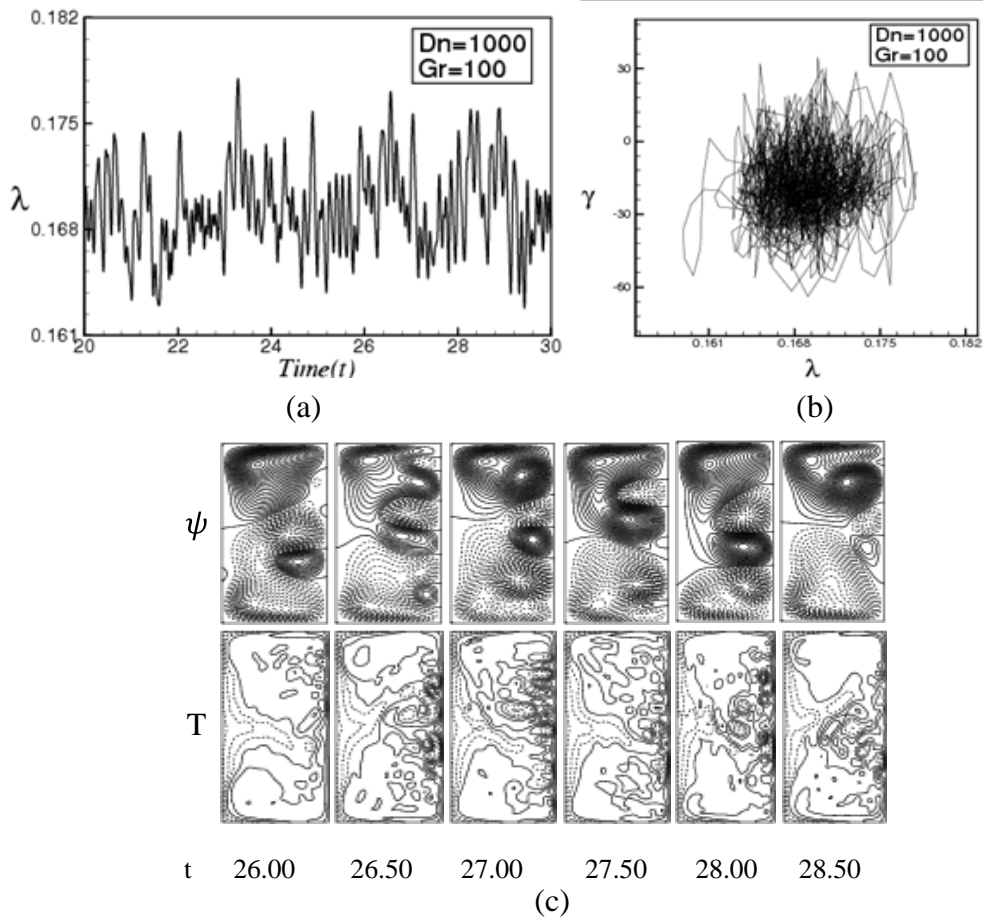


**Figure 12:** (a) Time evolution of  $\lambda$  at time  $2 \leq t \leq 10$ , (b) Phase space for  $Dn = 1000$  and  $Gr = 100, l = 2$ ,  
 (c) Secondary flow patterns (top) and Temperature profiles (bottom) for one period of oscillation for  
 same  $Dn, Gr$  and  $l$  at time  $26.0 \leq t \leq 28.5$ .

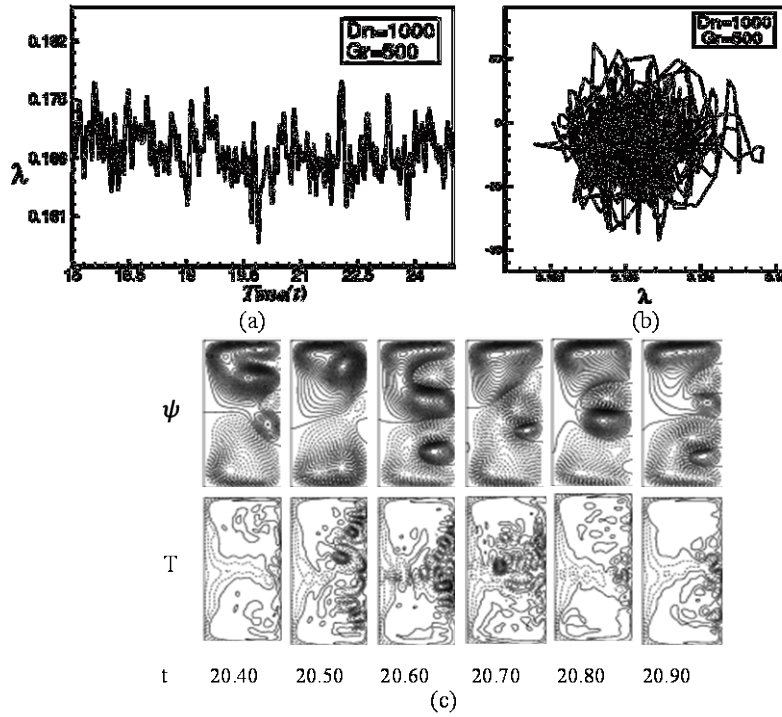


**Figure 13:** (a) Time evolution of  $\lambda$  at time  $15 \leq t \leq 25$ , (b) Phase space for  $Dn = 1000$  and  $Gr = 500, l = 2$ , (c) Secondary flow patterns (top) and Temperature profiles (bottom) for one period of oscillation for same  $Dn, Gr$  and  $l$  at time  $20.40 \leq t \leq 20.90$ .

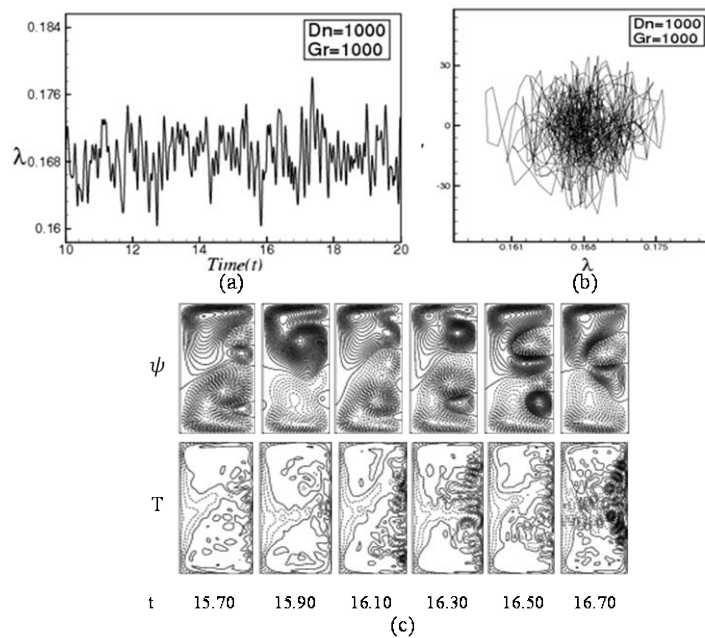


**Figure 14:** (a) Time evolution of  $\lambda$  at time  $10 \leq t \leq 20$ , (b) Phase space for  $Dn = 1000$  and  $Gr = 1000, l = 2$ , (c) Secondary flow patterns (top) and Temperature profiles (bottom) for one period of oscillation for same  $Dn, Gr$  and  $l$  at time  $15.70 \leq t \leq 16.70$ .

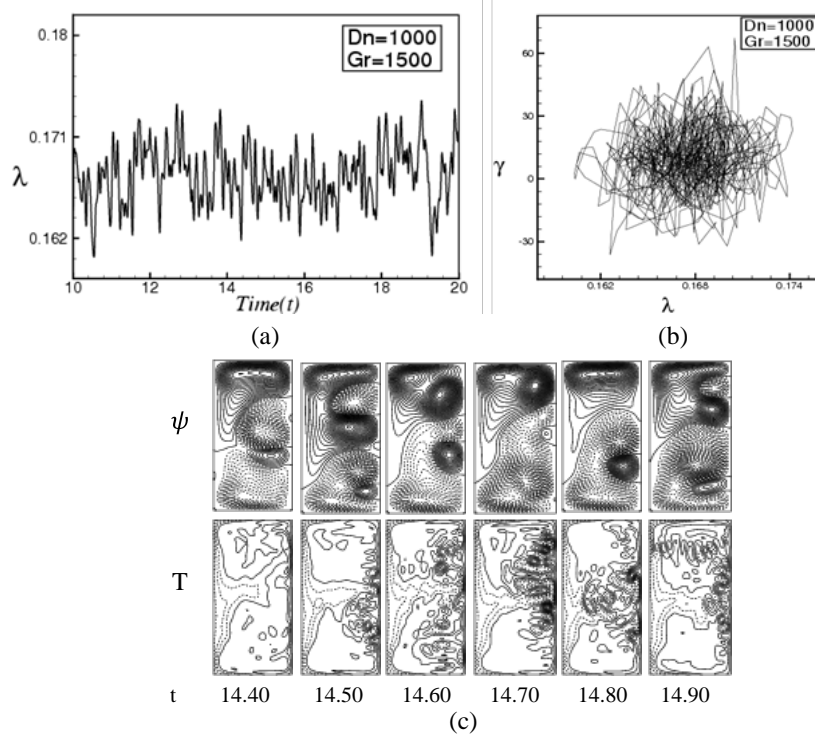


**Figure 15:** (a) Time evolution of  $\lambda$  at time  $10 \leq t \leq 20$ , (b) Phase space for  $Dn = 1000$  and  $Gr = 1500, l = 2$ , (c) Secondary flow patterns (top) and Temperature profiles (bottom) for one period of oscillation for same  $Dn, Gr$  and  $l$  at time  $14.40 \leq t \leq 14.90$

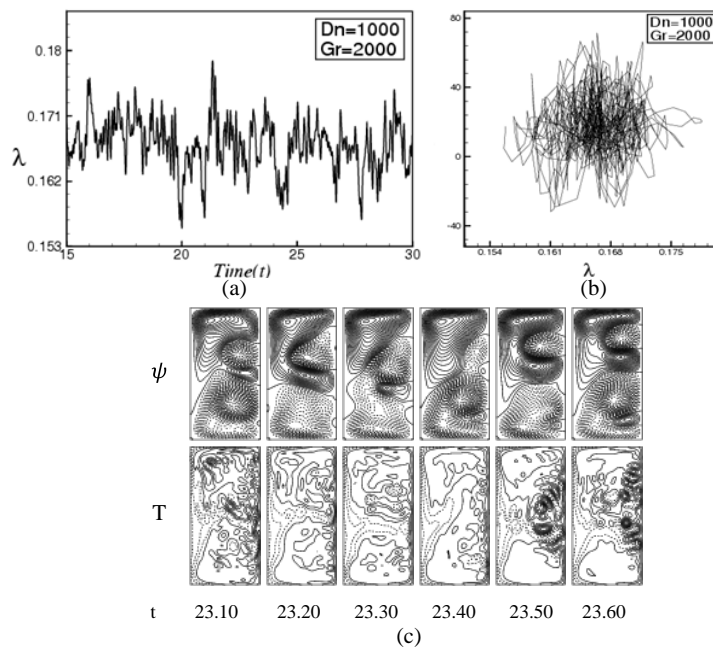


**Figure 16:** (a) Time evolution of  $\lambda$  at time  $15 \leq t \leq 30$ , (b) Phase space for  $Dn = 1000$  and  $Gr = 2000, l = 2$ , (c) Secondary flow patterns (top) and Temperature profiles (bottom) for one period of oscillation for same  $Dn, Gr$  and  $l$  at time  $23.10 \leq t \leq 23.60$ .

**4.2. Case II: Aspect Ratio  $l = 3$**

**4.2.1. Time evolution of the unsteady solutions**

We investigate time evolution of  $\lambda$  for the Dean numbers  $Dn = 100, 500$  and  $1000$  for the Grashof numbers  $100 \leq Gr \leq 2000$  for aspect ratio  $l = 3$ . We obtained the steady state solution for  $Dn = 100$  and  $Gr = 100, 2000$ . But at  $Dn = 100$  and  $Gr = 500, 1000, 1500$  the solution is periodic. We obtained the chaotic solution for  $Dn = 500$  at  $100 \leq Gr \leq 2000$ . We also obtained the chaotic solution at  $Dn = 1000$  for  $100 \leq Gr \leq 2000, l = 3$ .

Time evolution of the resistance coefficient  $\lambda$  at time  $12 \leq t \leq 18$  for  $Dn = 100$  and  $Gr = 100$  is shown in Fig. 18(a). We found that the flow is a steady-state solution. Secondary flow patterns and temperature profiles are shown in Fig. 18(b). We observe asymmetric two vortex solution for this case. It is found that the unsteady flow is periodic for  $Dn = 100$  and  $Gr = 500$  at time  $20 \leq t \leq 40$ , which is shown in Fig. 19(a). Secondary flow patterns and temperature profile. are shown in Fig. 19(b). We observe that the flow is an asymmetric two-vortex solution. In order to see the periodic behavior more clearly, the phase space of the time evolution of  $\lambda$  is also obtained as shown in Fig. 19(c). Time evolution of  $\lambda$  at time  $10 \leq t \leq 25$  for  $Dn = 100$  and  $Gr = 1000$  is shown in Fig. 20(a). It is found that the solution is multi-periodic oscillation. Secondary flow patterns and temperature profiles are shown in Fig. 20(b). Here we found asymmetric two-vortex solutions. In order to see the multi-periodic behavior more clearly, the phase space of the time evolution of  $\lambda$  is obtained as shown in Fig. 20(c). We find that the unsteady solution of the flow is periodic for  $Dn = 100$  and  $Gr = 1500$  as shown in Fig. 21(a). Secondary flow patterns and temperature profiles are shown in Fig. 21(b). We observe that the flow is an asymmetric two-vortex solution. In order to see the periodic behavior in more clearly, the phase space of the time evolution of  $\lambda$  as shown in Fig. 21(c). Time evolution of  $\lambda$  for  $Dn = 100$  and  $Gr = 2000$  is shown in Fig. 22(a). We found that the solution is steady-state solution. Secondary flow patterns and temperature profiles are shown in Fig. 22(b) for  $Dn = 100$  and  $Gr = 2000$ . We observe asymmetric two-vortex solution for this case.

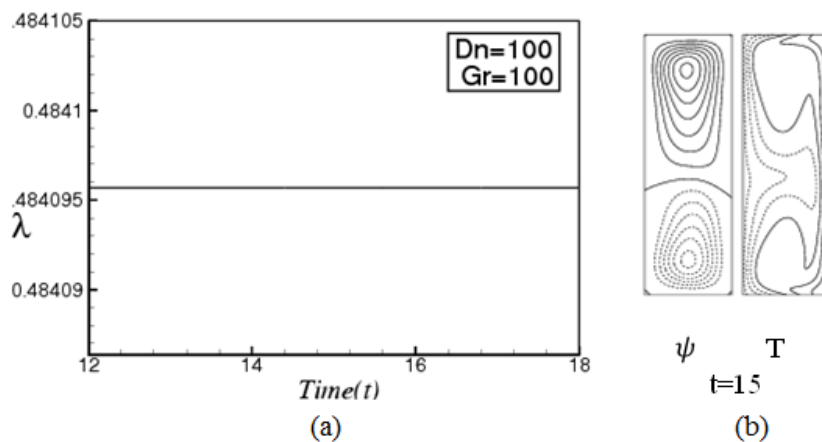


**Figure 17:** (a) Time evolution of  $\lambda$  at time  $12 \leq t \leq 18$ , (b) Secondary flow patterns (left) and Temperature

profiles (right) for  $Dn = 100$  and  $Gr = 100, l = 3$  at time  $t = 15$

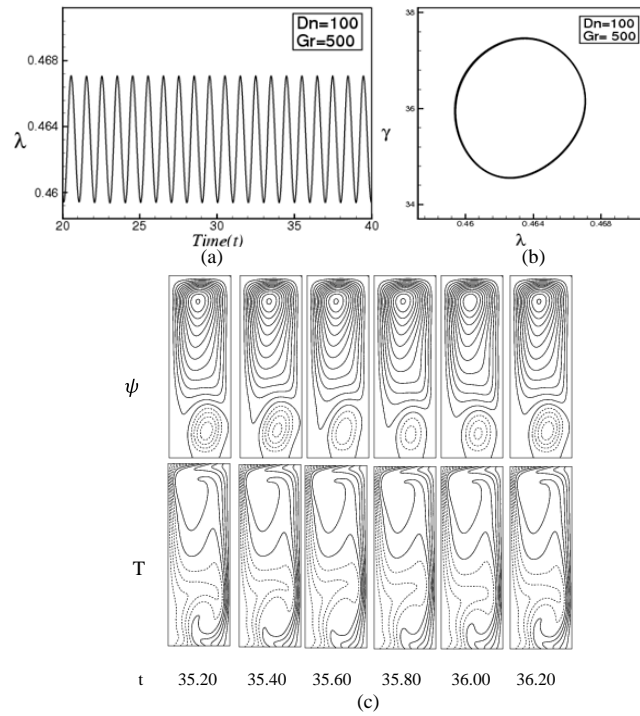


**Figure 18:** (a) Time evolution of  $\lambda$  at time  $20 \leq t \leq 40$ , (b) Phase space for  $Dn = 100$  and  $Gr = 500, l = 3$ , (c) Secondary flow patterns (top) and Temperature profiles (bottom) for one period of oscillation for same  $Dn, Gr$  and  $l$  at time  $35.20 \leq t \leq 36.20$ .

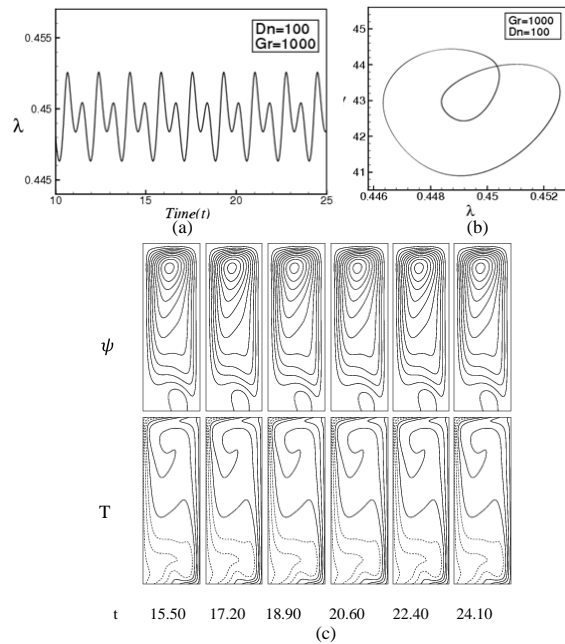


**Figure 19:** (a) Time evolution of  $\lambda$  at time  $10 \leq t \leq 25$ , (b) Phase space for  $Dn = 100$  and  $Gr = 1000, l = 3$ , (c) Secondary flow patterns (top) and Temperature profiles (bottom) for one period of oscillation for same  $Dn, Gr$  and  $l$  at time  $15.50 \leq t \leq 24.10$ .

same  $Dn, Gr$  and  $l$  at time  $15.50 \leq t \leq 24.10$ .

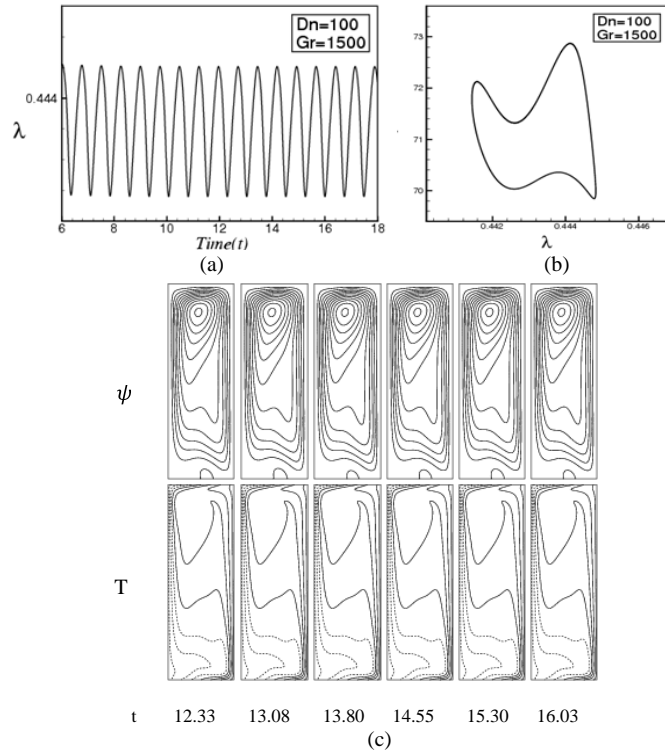


**Figure 20:** (a) Time evolution of  $\lambda$  at time  $6 \leq t \leq 18$ , (b) Phase space for  $Dn = 1000$  and  $Gr = 1500, l = 3$ , (c) Secondary flow patterns (top) and Temperature profiles (bottom) for one period of oscillation for same  $Dn, Gr$  and  $l$  at time  $12.33 \leq t \leq 16.03$ .

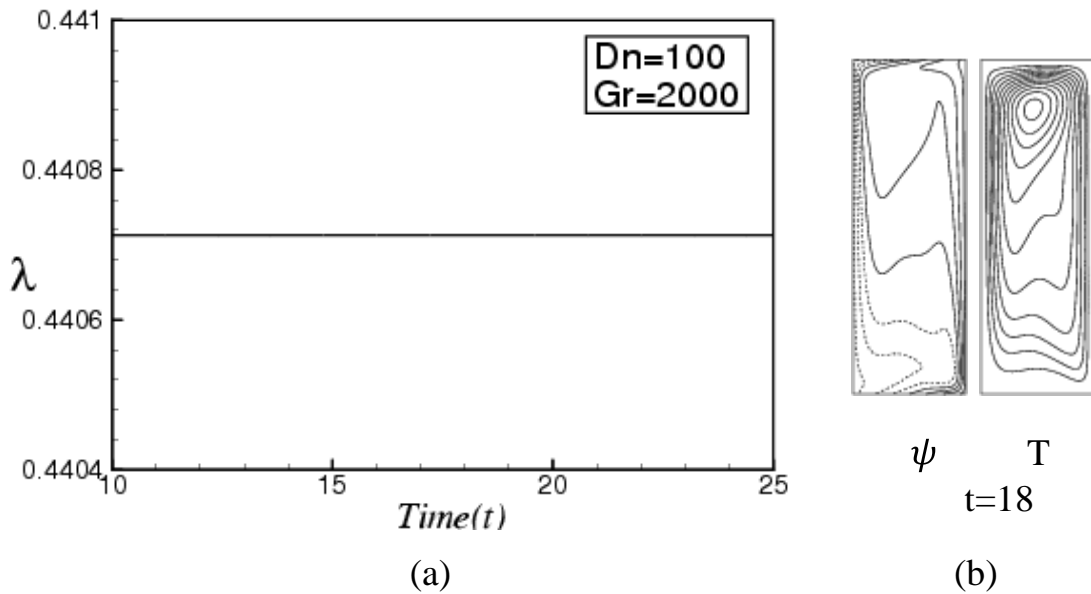


**Figure 21:** (a) Time evolution of  $\lambda$  at time  $10 \leq t \leq 25$ , (b) Secondary flow patterns (left) and Temperature

profiles (right) for  $Dn = 100$  and  $Gr = 2000, l = 3$  at time  $t = 18$ .

Time evolution of the resistance coefficient  $\lambda$  at time  $2.5 \leq t \leq 9.5$  for  $Dn = 500$  and  $Gr = 100$  is shown in Fig. 23(a). We found that the solution is a chaotic flow. Secondary flow patterns and temperature profile are shown in Fig. 23(b). Here we found symmetric four-, five- and six-vortex solutions. In order to see the chaotic behavior more clearly, the phase space of the time evolution of  $\lambda$  is shown in Fig. 23(c). It is found that the unsteady solution of the flow is chaotic for  $Dn = 500$  and  $Gr = 500$ , which is shown in Fig. 24(a). Secondary flow patterns and temperature profile are shown in Fig. 24(b). We observe asymmetric three, four and five vortex solution. In order to see the chaotic behavior in more clearly, the phase space of the time evolution of  $\lambda$  as shown in Fig 24(c). Time evolution of the resistance coefficient  $\lambda$  at time  $5 \leq t \leq 9$  for  $Dn=500$  and  $Gr.=1000$  is shown in Fig. 25(a). We found that the solution is chaotic. Secondary flow patterns and temperature profile is shown in Fig 25(b). Here we found symmetric four-, five- and six-vortex solutions. In order to see the chaotic behavior more clearly, the phase space of the time evolution of  $\lambda$  is also drawn as shown in Fig. 25(c). Next, we obtained the unsteady solution of the flow and we find that the flow is chaotic for  $Dn = 500$  and  $Gr = 1500$  as shown in Fig. 26(a). Secondary flow patterns and temperature profile is shown in Fig 26(b). We observe that the flow is an asymmetric five-, six- and seven-vortex solution. In order to see the chaotic behavior more clearly, the phase space of the time evolution of  $\lambda$  is shown in Fig. 26(c). Then we calculate the unsteady solution of the flow for  $Dn = 500$  and  $Gr = 2000$  and we find that the flow is chaotic, which is shown in Fig. 27(a). Secondary flow patterns and temperature profile is shown in Fig 27(b). We observe that there occurs asymmetric five-, six- and seven-vortex solution. In order to see the chaotic behavior more clearly, the phase space of the time evolution of  $\lambda$  is also obtained as shown in Fig. 27(c).

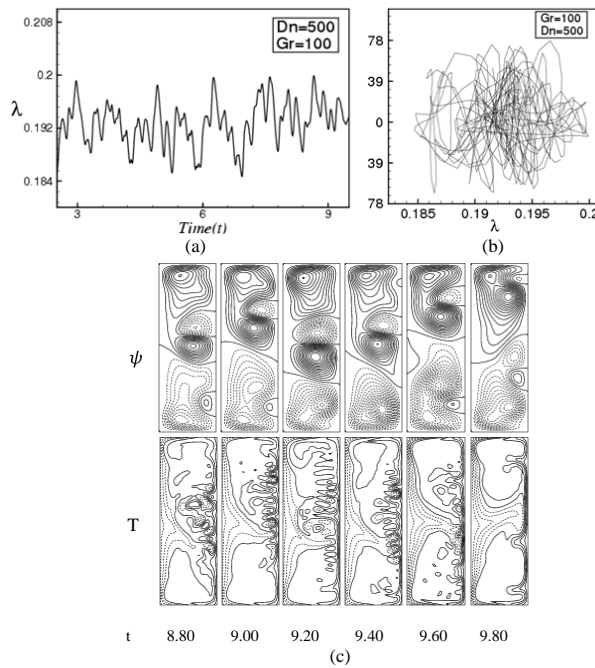
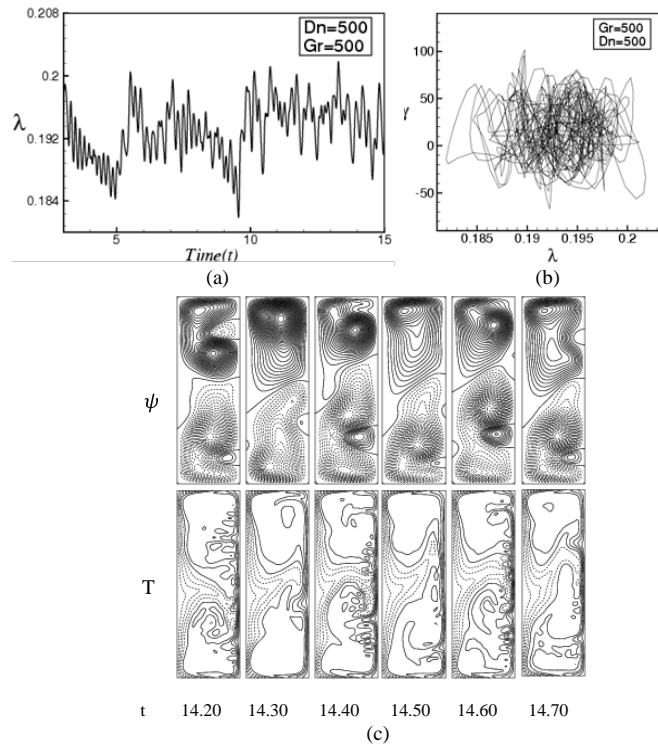
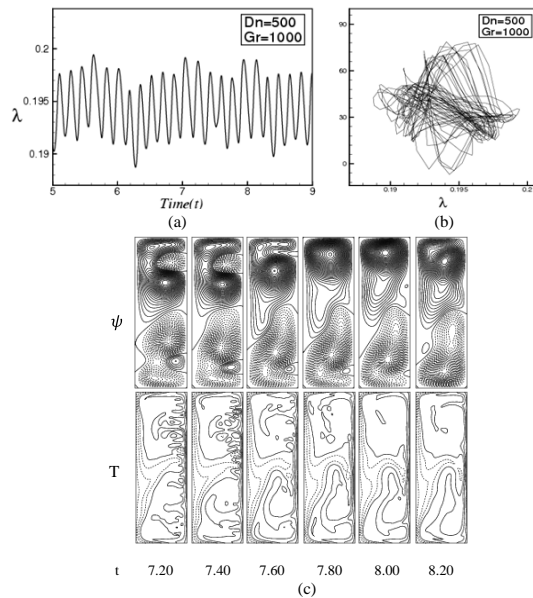


Figure 22: (a) Time evolution of  $\lambda$  at time  $6 \leq t \leq 18$ , (b) Phase space for  $Dn = 500$  and  $Gr = 100, l = 3$ ,

(c) Secondary flow patterns (top) and Temperature profiles (bottom) for one period of oscillation for same  $Dn, Gr$  and  $l$  at time  $8.80 \leq t \leq 9.80$ .



**Figure 23:** (a) Time evolution of  $\lambda$  at time  $3 \leq t \leq 15$ , (b) Phase space for  $Dn = 500$  and  $Gr = 500, l = 3$ , (c) Secondary flow patterns (top) and Temperature profiles (bottom) for one period of oscillation for same  $Dn, Gr$  and  $l$  at time  $14.20 \leq t \leq 14.70$ .



**Figure 24:** (a) Time evolution of  $\lambda$  at time  $6 \leq t \leq 18$ , (b) Phase space for  $Dn = 500$  and  $Gr = 500, l = 3$ , (c)

Secondary flow patterns (top) and Temperature profiles (bottom) for one period of oscillation for same  $Dn, Gr$  and  $l$  at time  $7.20 \leq t \leq 8.20$ .

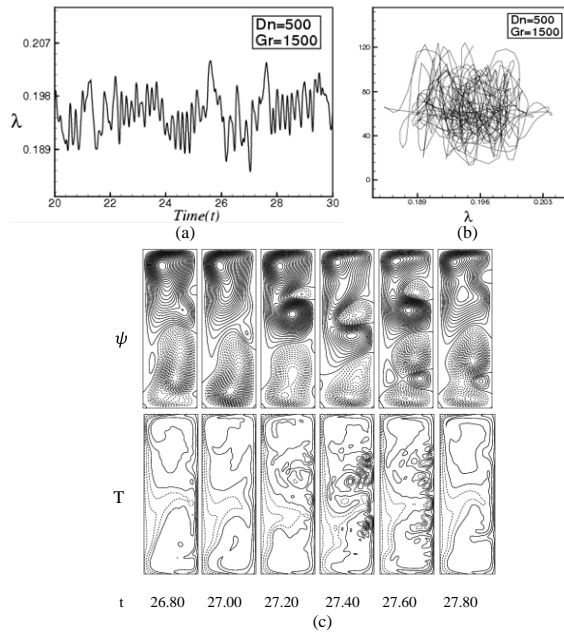


**Figure 25:** (a) Time evolution of  $\lambda$  at time  $6 \leq t \leq 18$ . (b) Phase space for  $Dn = 500$  and  $Gr = 1500, l = 3$ , (c) Secondary flow patterns (top) and Temperature profiles (bottom) for one period of oscillation for same  $Dn, Gr$  and  $l$  at time  $26.80 \leq t \leq 27.80$ .

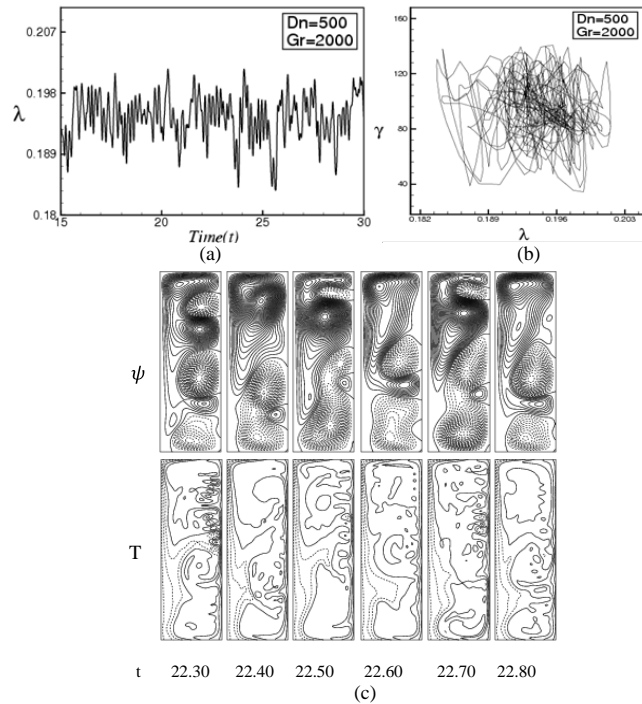


**Figure 26:** (a) Time evolution of  $\lambda$  at time  $15 \leq t \leq 30$ , (b) Phase space for  $Dn = 500$  and  $Gr = 2000, l = 3$ ,

(c) Secondary flow patterns (top) and Temperature profiles (bottom) for one period of oscillation for same  $Dn, Gr$  and  $l$  at time  $22.30 \leq t \leq 22.80$ .

Here we investigate time evolution of the resistance coefficient  $\lambda$  for  $Dn=1000$  and  $Gr=100$  as shown in Fig 28(a). We found that the flow is chaotic. Secondary flow patterns and temperature profile are shown in Fig. 28(b). Here we found symmetric five and six vortex solutions. In order to see the chaotic behavior more clearly, the phase space of the time evolution of  $\lambda$  is shown in Fig. 28(c). We investigate the unsteady solution of the flow for  $Dn = 1000$  and  $Gr = 500$  and it is found that the flow is chaotic as shown in Fig. 29(a) for time  $0 \leq t \leq 17$ . Secondary flow patterns and temperature profile are shown in Fig 29(b). We observe asymmetric six and seven vortex solution. In order to see the chaotic behavior in more clearly, the phase space of the time evolution of  $\lambda$  as shown in Fig 29(c). Time evolution of the resistance coefficient  $\lambda$  at time  $30 \leq t \leq 40$  for  $Dn = 1000$  and  $Gr = 1000, 1500$  are shown in Figs. 30(a) and 31(a) respectively. We found that the solution is chaotic. Secondary flow patterns and temperature profile are shown in Fig 30(b) and 31(b) respectively. Here we found symmetric five, six and seven vortex solutions. In order to see the chaotic behavior in more clearly, the phase space of the time evolution of  $\lambda$  as shown in Fig 30(c) and 31(c) respectively. Unsteady solution of the flow is chaotic for  $Dn = 1000$  and  $Gr = 2000$  at time  $15 \leq t \leq 35$  is shown in Fig 32(a). Secondary flow patterns and temperature profile is shown in Fig 32(b). We observe asymmetric five, six and seven vortex solution. In order to see the chaotic behavior more clearly, the phase space of the time evolution of  $\lambda$  is obtained as shown in Fig. 32(c).

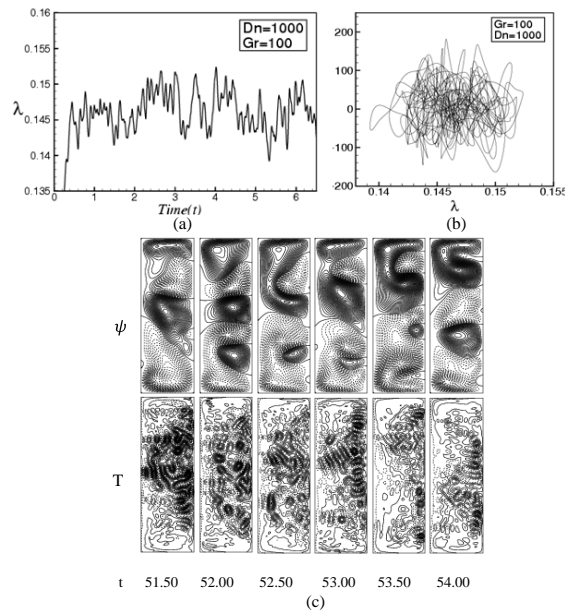


**Figure 27:** (a) Time evolution of  $\lambda$  at time  $0 \leq t \leq 7$ , (b) Phase space for  $Dn = 1000$  and  $Gr = 100, l = 3$ ,

(c) Secondary flow patterns (top) and Temperature profiles (bottom) for one period of oscillation for same  $Dn, Gr$  and  $l$  at time  $51.50 \leq t \leq 54.00$ .

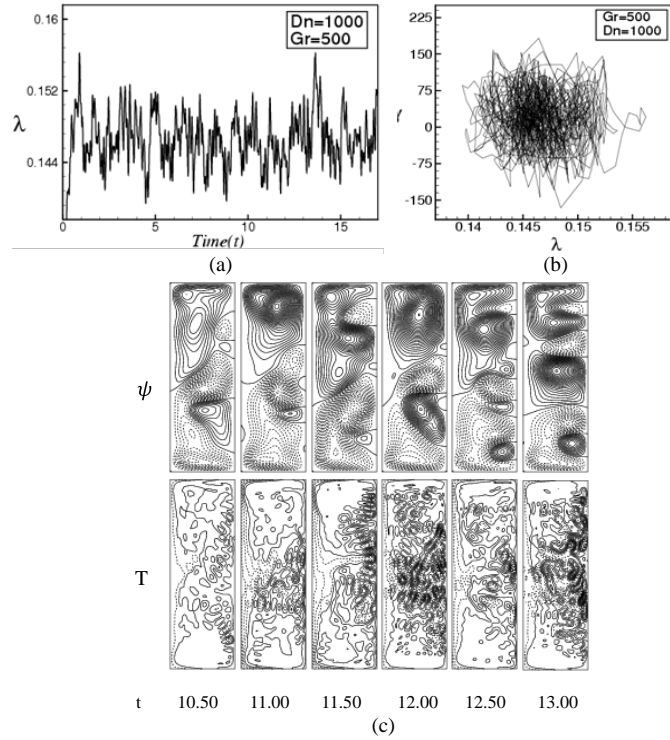


**Figure 28:** (a) Time evolution of  $\lambda$  at time  $0 \leq t \leq 16$ , (b) Phase space for  $Dn = 1000$  and  $Gr = 500, l = 3$ ,

(c) Secondary flow patterns (top) and Temperature profiles (bottom) for one period of oscillation for same  $Dn, Gr$  and  $l$  at time  $10.50 \leq t \leq 13.00$  for  $l = 3$ .

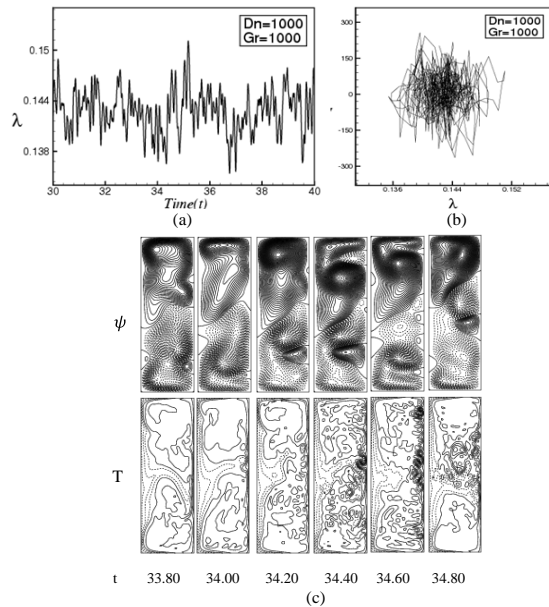


**Figure 29:** (a) Time evolution of  $\lambda$  at time  $30 \leq t \leq 40$ , (b) Phase space for  $Dn = 1000$  and  $Gr = 1000, l = 3$ , (c) Secondary flow patterns (top) and Temperature profiles (bottom) for one period of oscillation for same  $Dn, Gr$  and  $l$  at time  $33.80 \leq t \leq 34.80$ .

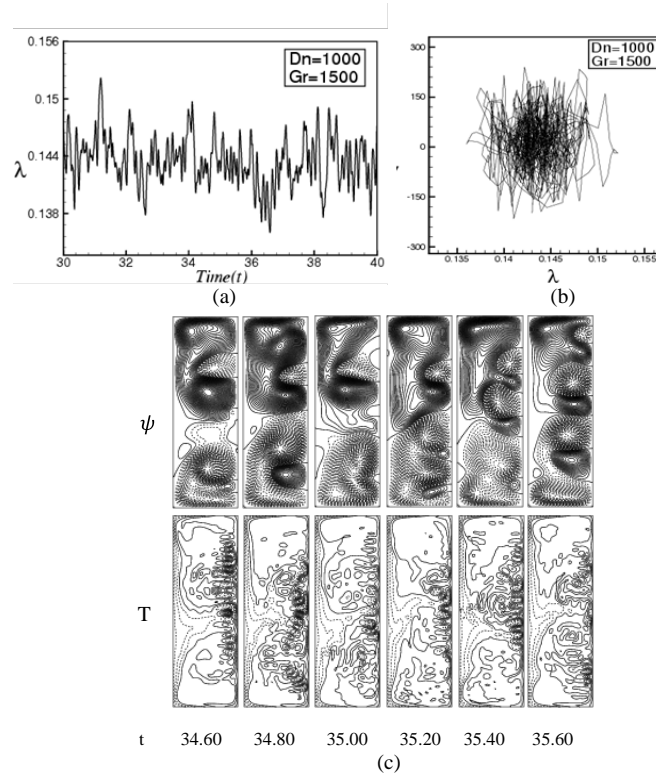


**Figure 30(a):** Time evolution of  $\lambda$  at time  $30 \leq t \leq 40$  for  $Dn = 1000$  and  $Gr = 1500$  for the aspect ratio  $l = 3$ , (c) Secondary flow patterns (top) and Temperature profiles (bottom) for one period of oscillation for same  $Dn, Gr$  and  $l$  at time  $34.60 \leq t \leq 35.60$ .

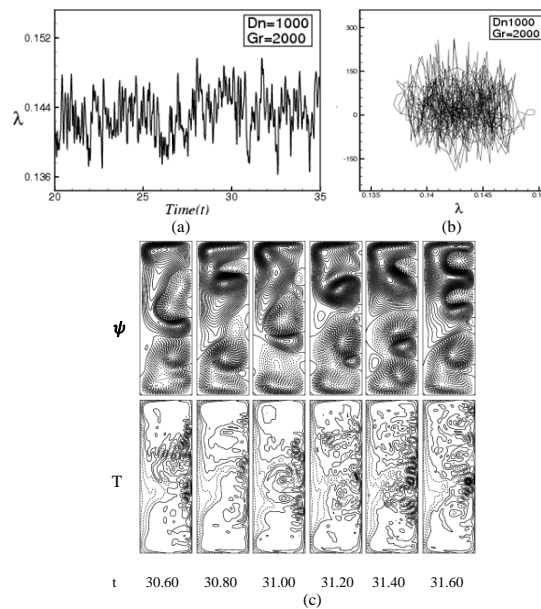


**Figure 31(a):** Time evolution of  $\lambda$  at time  $20 \leq t \leq 35$  for  $Dn = 1000$  and  $Gr = 2000$  for the aspect ratio  $l = 3$ , (c) Secondary flow patterns (top) and Temperature profiles (bottom) for one period of oscillation for same  $Dn, Gr$  and  $l$  at time  $30.60 \leq t \leq 31.60$ .

**4.2.2. Unsteady solutions in Dean vs Grashof Plane**

Here, the distribution of the unsteady solutions, obtained by the time evolution calculations of the solutions, are presented in the phase diagram in the Dn-Gr plane for  $0 < Dn \leq 1000$  and  $100 \leq Gr \leq 2000$  for the aspect ratios 2 and 3 in Figs. 33(a) and 33(b) respectively. In these figures, the circle denotes steady-state solution, the cross periodic solutions and the triangle chaotic solutions. As seen in Fig. 33(a), the steady-state solution turns into chaotic solution for small ( $Gr = 100, 500$ ) and large Grashof numbers ( $Gr = 2000$ ) for the case of aspect ratio 2, for moderate Grashof numbers, however, steady-state solution turns into chaotic solution through periodic solution, if the Dean number is increased. For the aspect ratio 3, we find that the steady-state solution turns into chaotic solution for  $Gr = 100, 500, 1500$  and  $2000$ , but at  $Gr = 1000$ , the steady-state solution turns into chaotic solution through periodic solution, if the Dean number is increased. Thus we get a through knowledge about the complete unsteady flow behavior of the present study from Figure 33.

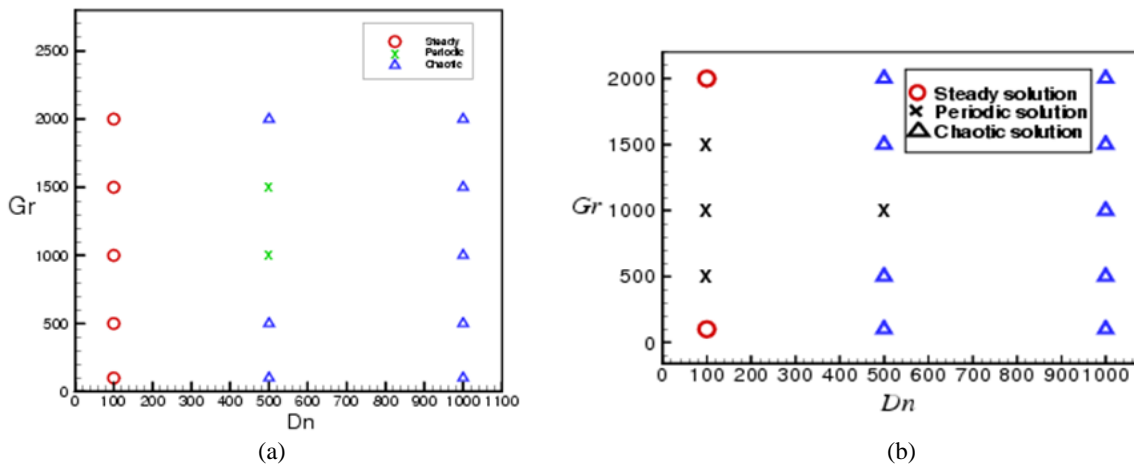


**Figure 32:** Graphical representation of unsteady solutions for  $100 \leq Dn \leq 1000$  and  $100 \leq Gr \leq 2000$  (a) for aspect ratio 2 and (b) for aspect ratio 3 respectively.

**5. Conclusion**

Here, we have studied a comprehensive numerical study of the time dependent solutions of the flow characteristics through a curved rectangular cross-section for various aspect ratios. Numerical calculations are carried out by using the spectral method over a wide range of the Dean number for a fixed curvature  $\delta = 0.1$ . In the present study, however, we performed time evolution calculations of the unsteady solutions through a curved rectangular flow for the aspect ratios 2, and 3.

In the present article, we studied the time-dependent solutions of the resistance coefficient  $\lambda$  over a wide range of the Dean number  $100 \leq Dn \leq 1000$  for the rectangular cross-section of aspect ratio  $l = 2$  and  $l = 3$ . At first, we investigated the unsteady solutions of the curved rectangular cross-section flow of aspect ratio  $l = 2$ . We found that the unsteady flow is steady-state for  $Dn=100$  at  $Gr = 100, 500, 1500, 2000$ . But only the flow

is periodic for  $Dn = 100$  at  $Gr = 1000$ . We find that the unsteady flow is periodic for  $Dn = 500$  and  $Gr = 1000$ . The unsteady flow is multi-periodic for  $Dn = 500$  and  $Gr = 1500$ . It is also found that the solution is chaotic for  $Dn = 500$  at  $Gr = 100, 500, 2000$ . Here we find that the flow is chaotic for  $Dn = 1000$  at  $Gr$  number varies from  $100 \leq Gr \leq 2000$ . We obtained secondary flow patterns and temperature profiles for all types of solution and for the steady-state solution, we found two vortex solutions, while for the periodic flow, we obtained two vortex solution. In this regard, it should be noted that, the multi-periodic solution, obtained in the present study at the above-mentioned Dean numbers, they do not possess the same characteristics. When the flow is chaotic we get four- and five- vortex solution.

Then we studied the time evolution of  $\lambda$  for a wide range of the Dean number  $100 \leq Dn \leq 1000$  and the range of Grashof Number  $100 \leq Gr \leq 2000$  for the curved rectangular cross-section flow of aspect ratio 3 and we found that the unsteady flow is steady-state solution for  $Dn = 100$  at  $Gr = 100, 2000$ . However, the unsteady flow is periodic for  $Dn = 100$  at  $Gr = 500, 1000, 1500$ .

We found that the unsteady flow is chaotic for  $Dn = 500, 1000$  for all the grashof numbers investigated in this study. Contours of secondary flow patterns and temperature profiles are also obtained for all solutions. It is found that the periodic solution oscillates between asymmetric two-, and four-vortex solutions. When the flow is chaotic we get five, six and seven vortex solutions. The temperature distribution is consistent with the secondary vortices generated at the outer wall of the duct. It is found that the temperature passes significantly from the heated wall to the fluid as the secondary vortices increases.

## References

- [1] Dean, W. R., and J. M. Hurst. "Note on the motion of fluid in a curved pipe." *Philos Mag*, 4:208-23
- [2] Berger, S. A., L. Talbot, and L. S. Yao. "Flow in curved pipes." *Annual review of fluid mechanics* 15.1 (1983): 461 – 512.
- [3] Ito, Hidesato. "Flow in curved pipes." *JSME international journal* 30.262 (1987): 543 – 552.
- [4] Nandakumar, K. "Swirling flow and heat transfer in coiled and twisted pipes." *Advances in transport processes* 4 (1986): 49 – 112.
- [5] Yanase, Shinichiro, Yoshito Kaga, and Ryuji Daikai. "Laminar flows through a curved rectangular duct over a wide range of the aspect ratio." *Fluid Dynamics Research* 31.3 (2002): 151.
- [6] Zhang, J.S., Zhang, B.Z. and Jü, J. (2001) Fluid Flow in a Rotating Curved Rectangular Duct. *International Journal of Heat and Fluid Flow*, 22, 583-592.
- [7] Winters, Keith H. "A bifurcation study of laminar flow in a curved tube of rectangular cross-section." *Journal of Fluid Mechanics* 180 (1987): 343 – 369.
- [8] Mondal R. N., Kaga Y., Hyakutake, T and Yanase, S. "Unsteady solutions and the bifurcation diagram for the flow through a curved square duct", *Fluids Dynamics Research* 39 (2007): 413 – 446.

- [9] Wang, Liqiu, and Tianliang Yang. "Periodic oscillation in curved duct flows." *Physica D: Nonlinear Phenomena* 200.3-4 (2005): 296 – 302.
- [10] Yanase, Shinichiro, and Koji Nishiyama. "On the bifurcation of laminar flows through a curved rectangular tube." *Journal of the Physical Society of Japan* 57.11 (1988): 3790 – 3795.
- [11] Wang, Liqiu, and Fang Liu. "Forced convection in tightly coiled ducts: Bifurcation in a high Dean number region." *International Journal of Non-Linear Mechanics* 42.8 (2007): 1018 – 1034.
- [12] Mondal, R. N., Islam, S., Uddin, K., & Hossain, A. "Effects of aspect ratio on unsteady solutions through curved duct flow." *Applied Mathematics and Mechanics* 34.9 (2013): 1107 – 1122.
- [13] Chandratilleke, Tilak T. "Numerical prediction of secondary flow and convective heat transfer in externally heated curved rectangular ducts." *International Journal of Thermal Sciences* 42.2 (2003): 187 – 198.
- [14] Norouzi M, Kayhani M. H, Shu C, Nobari M. R. H. "Flow of second-order fluid in a curved duct with square cross section", *J Non-Newtonian Fluid Mech* 165(2010): 323 – 339.
- [15] Chandratilleke T. T, Nadim N., Narayanaswamy R. "Vortex structure-based analysis of laminar flow behavior and thermal characteristics in curved ducts", *Int J Thermal Sci*, 59(2012): 75 – 86.
- [16] Zhang L. J, Zhang W. P, Ming P. J. "Numerical simulation of secondary flow in a curved square duct", *Applied Mathematics and Materials*, 681(2014): 33 – 40.
- [17] Mondal, R. N., Islam, M. Z. and Pervin, R. "Combined effects of centrifugal and coriolis instability of the flow through a rotating curved duct of small curvature", *Procedia Engineering*, 90(2014): 261 – 267.
- [18] Yamamoto, K., Wu, X., Nozaki, K. and Hayamizu, Y. (2006) Visualization of Taylor-Dean Flow in a Curved Duct of Square Cross-Section. *Fluid Dynamics Research*, 38, 1-18
- [19] Nobari, M.R.H., Nousha, A. and Damangir, E. (2009) A Numerical Investigation of Flow and Heat Transfer in Ro-tating U-Shaped Square Ducts. *International Journal of Thermal Sciences*, 48, 590-601.
- [20] Li Y, Wang X, Yuan S, Tan S. K. "Flow Development in Curved Rectangular Ducts with Continuously Varying Curvature", *Experimental Thermal and Fluid Science*, 75(2016): 1 – 15.
- [21] Gottlieb D and Orazag SA. "Numerical Analysis of Spectral Methods", *Society of Industrial and Applied Mathematics, Philadelphia, USA* (1977).
- [22] Keller H. B. "Lectures on Numerical Methods in Bifurcation Problems", *Springer, Berlin* (1987).